Journal of Computational Physics 348 (2017) 139–150

Contents lists available at ScienceDirect

Journal of Computational Physics

www.elsevier.com/locate/jcp

Impact of parametric uncertainty on estimation of the energy deposition into an irradiated brain tumor

Søren Taverniers [b], Daniel M. Tartakovsky [a,*]

[a] Department of Energy Resources Engineering, Stanford University, 367 Panama Street, Stanford, CA 94305, USA
[b] Department of Mechanical and Aerospace Engineering, University of California, San Diego, 9500 Gilman Drive, MC 0411, La Jolla, CA 92093, USA

ARTICLE INFO

Article history:
Received 1 September 2016
Received in revised form 21 March 2017
Accepted 4 July 2017
Available online 12 July 2017

Keywords:
Brain tumor
Radiation therapy
Radiation diffusion
Nonlinear diffusion
Uncertainty quantification

ABSTRACT

Predictions of the total energy deposited into a brain tumor through X-ray irradiation are notoriously error-prone. We investigate how this predictive uncertainty is affected by uncertainty in both the location of the region occupied by a dose-enhancing iodinated contrast agent and the agent's concentration. This is done within the probabilistic framework in which these uncertain parameters are modeled as random variables. We employ the stochastic collocation (SC) method to estimate statistical moments of the deposited energy in terms of statistical moments of the random inputs, and the global sensitivity analysis (GSA) to quantify the relative importance of uncertainty in these parameters on the overall predictive uncertainty. A nonlinear radiation–diffusion equation dramatically magnifies the coefficient of variation of the uncertain parameters, yielding a large coefficient of variation for the predicted energy deposition. This demonstrates that accurate prediction of the energy deposition requires a proper treatment of even small parametric uncertainty. Our analysis also reveals that SC outperforms standard Monte Carlo, but its relative efficiency decreases as the number of uncertain parameters increases from one to three. A robust GSA ameliorates this problem by reducing this number.

1. Introduction

In addition to surgery and chemotherapy, radiotherapy is one of the main treatment methods for brain tumors. Its goal is to either destroy a tumor or to prevent it from developing further, and it may serve as the only treatment (e.g., for inoperable tumors) or in combination with surgery (to kill any remaining microscopic tumor cells). X-rays are the primary type of radiation involved in radiotherapy; their interaction with the medium in which they propagate produces energetic electrons which, in turn, lose their energy as they are slowed down through collisions. To enhance the energy dose absorbed by the tumor, a contrast agent based on a substance with high atomic number Z, such as iodine, may be injected [1]. This increases the photo-electric absorption of X-rays (the photo-electric mass attenuation coefficient increases strongly with Z [2]), one of the main radiation-matter interactions at photon energies in the keV range. The photo-electric effect may also result in the emission of Auger electrons that can equally contribute to the overall energy deposition. Within the keV energy range, X-rays are also likely to undergo Compton scattering and transfer their energy to existing free electrons; however, this process has a mass attenuation coefficient that is nearly independent of Z [2].

* Corresponding author.
E-mail address: tartakovsky@stanford.edu (D.M. Tartakovsky).

http://dx.doi.org/10.1016/j.jcp.2017.07.008
0021-9991/

Temporal and K-edge subtraction methods [3] are often used to infer the contrast agent's concentration within the brain and tumor, which inevitably introduces measurement errors and uncertainty in the agent's concentration estimates. As the agent preferentially accumulates in the tumor interstitium due to the increased permeability of the broken blood-brain barrier, it diffuses into the surrounding healthy brain tissue, introducing uncertainty in the agent's spatial extent during the irradiation procedure. These and other sources of parametric and structural uncertainty render simulation-based predictions of the amount and spatial distribution of the energy deposited in the tumor uncertain. Adverse effects of predictive uncertainty on the efficacy of radiotherapy and clinical outcomes have been well documented [e.g., [4–8]].

The effects of iodine concentration on dose enhancement [9] and the uniformity of the dose distribution within the tumor [10] have been analyzed using the Monte Carlo N-particle (MCNP) method [11,12]. The latter simulates trajectories of small photon packets whose energy and propagation direction are statistically selected. The method was used to model interactions of X-ray photons with the brain/tumor matter, and transport of electrons released as a result of these interactions. MCNP simulations have high fidelity, but require a large number of runs due to the slow convergence of Monte Carlo simulations (MCS) and often become computationally prohibitive.

Alternative uncertainty quantification techniques aim to outperform MCS in terms of computational efficiency. They are often subdivided into intrusive (moment differential equations [e.g., [13]], stochastic Galerkin methods [e.g., [14]], etc.) and nonintrusive (stochastic collocation or SC [e.g., [15]], multilevel Monte Carlo [e.g., [16]], etc.) groups. The former strategies require one to modify an underlying (deterministic) solver but are often more robust and computationally efficient, while the latter rely on repeated runs of the existing solver and amount to "accelerated" (relative to standard MCS) sampling of the parameter space. We adopt the second strategy because it has the best chance of being adopted in design of a radiotherapy treatment.

Depending on the number of uncertain parameters and/or the degree of a problem's nonlinearity, SC might or might not outperform MCS [17]. We investigate the relative performance of these two methods in the context of a two-dimensional, flux-limited radiation–diffusion equation [18,19], which provides a continuum-level description of energy deposition into an X-ray irradiated brain tumor. We assume that the X-rays are monochromatic and in the keV range [20], and represent the region over which the contrast agent spreads out as a square inset in a larger square domain representing the brain. The coordinates of the center of this inset and the effective atomic number in this area, which depends on the agent's concentration, are uncertain and treated as uniformly distributed random variables.

A mathematical formulation of this problem is given in Section 2. Section 3 contains a description of the spatial discretization method and time advancement algorithm used to obtain a numerical solution to the equilibrium radiation–diffusion equation, as well as the statistical moment estimators of the deposited energy computed with SC and MCS. In Section 4 we perform a number of numerical experiments, whose goal is to ascertain the relative performance of these two methods. Results of a global sensitivity analysis, whose aim is to reduce the number of uncertain parameters used in SC, are presented in Section 5. Major conclusions drawn from these experiments are summarized in Section 6.

2. Problem formulation

Let us assume that the collisional mean free path of the photons is small relative to the system (i.e., brain) size, and that the radiation field is isotropic and in thermal equilibrium with the medium. Then transport of monochromatic[1] X-rays through a planar (two-dimensional) brain's segment $\mathcal{D}$ is described by an equilibrium radiation–diffusion equation [19,21]

$$\frac{\partial E}{\partial t} = \nabla \cdot [D(E, \nabla E, \mathbf{x}) \nabla E], \qquad \mathbf{x} \in \mathcal{D}, \quad t > 0. \tag{1a}$$

Here $E(\mathbf{x}, t)$ is the radiation energy density at point $\mathbf{x} = (x_1, x_2)^\top$ and time t, and D is the diffusion coefficient given by [21]

$$D(E, \nabla E, \mathbf{x}) = \frac{cE}{\gamma E / D_Z + |\nabla E|}, \tag{1b}$$

where c is the speed of light, γ combines a number of physical constants and ensures dimensional correctness, $D_Z = Z^{-3} E^{3/4}$ is proportional to the diffusion coefficient without flux-limiting, and $Z(\mathbf{x})$ is the effective atomic number. The two-dimensional square domain $\mathcal{D} \equiv (0, L) \times (0, L)$ contains a subregion $\mathcal{T} = [L/2 - w/2, L/2 + w/2] \times [L/2 - w/2, L/2 + w/2]$ with $w = L/5$, representing the tumor (Fig. 1). Upon injection, an iodinated contrast agent spreads over a subdomain $\mathcal{D}_2 = \mathcal{D} \setminus \mathcal{D}_1 = [c_1 - w/2, c_1 + w/2] \times [c_2 - w/2, c_2 + w/2]$, which may fully or partially overlap with $\mathcal{T}$ depending on the values of c_1 and c_2 (Fig. 1). The medium in $\mathcal{D}_2$ has an uncertain effective[2] atomic number Z_2, which is smaller than the atomic number of the contrast agent Z_{ca} (for iodine, $Z_{\text{ca}} = 53$) and larger than the effective atomic number of either healthy brain tissue (for $\mathbf{x} \in \mathcal{D}_2 \setminus \mathcal{T}$) or tumor matter (for $\mathbf{x} \in \mathcal{D}_2 \cap \mathcal{T}$). Since the effective atomic numbers of both healthy and tumorous brain matter are much smaller than Z_{ca}, we assume them both to equal that of healthy brain tissue. The latter

[1] The use of monochromatic radiation, in which all photons have an identical energy, obviates the need for frequency-averaging of the spectral radiation energy density, i.e., for a gray approximation.

[2] A composite medium may be characterized by an effective atomic number, which depends on its composition and the energy of the X-ray photons.

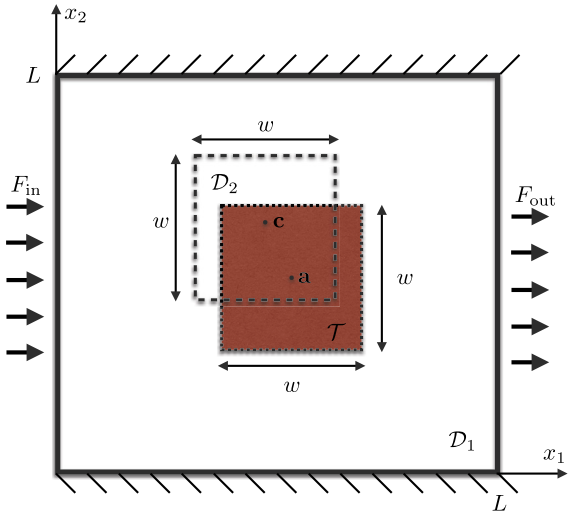

Fig. 1. Computational domain $\mathcal{D}$ for the radiation–diffusion problem. Subdomains $\mathcal{D} \setminus \mathcal{T}$, $\mathcal{T}$ and $\mathcal{D}_2$ represent healthy brain tissue, tumor and region occupied by the contrast agent, respectively.

is set to $Z_{\text{hb}} = 5$, which is an average value for grey/white human brain matter over the keV range of photon energies [22]. Hence,

$$Z(\mathbf{x}) = \begin{cases} Z_{\text{hb}} & \text{for } \mathbf{x} \in \mathcal{D}_1 \\ Z_{\text{hb}} < Z_2 < Z_{\text{ca}} & \text{for } \mathbf{x} \in \mathcal{D}_2. \end{cases} \tag{1c}$$

Equation (1) is subject to the initial condition

$$E(\mathbf{x}, 0) = E_{\text{in}}(\mathbf{x}), \qquad \mathbf{x} \in \mathcal{D} \tag{2a}$$

and boundary conditions (see Fig. 1)

$$\left[E - 2D\frac{\partial E}{\partial x_1}\right]_{x_1=0} = 4F_{\text{in}}, \qquad \left[E + 2D\frac{\partial E}{\partial x_1}\right]_{x_1=L} = 4F_{\text{out}}, \tag{2b}$$

$$\frac{\partial E}{\partial x_2} = 0, \qquad x_2 = 0 \text{ and } L, \tag{2c}$$

where F_{in} and F_{out} are the half-range fluxes along the domain's inlet ($x_1 = 0$) and outlet ($x_1 = L$), respectively. Derivation of the radiation (Marshak) boundary conditions (2b) can be found in, e.g., [19].

A quantity of interest (QoI) in this problem is the total energy deposition in $\mathcal{T}$ over a time horizon T,

$$E_{\text{tot}} = \int_0^T \int_{\mathcal{T}} \dot{E}_{\text{abs}}(\mathbf{x}, t) \mathrm{d}\mathbf{x}\mathrm{d}t. \tag{3a}$$

Here $\dot{E}_{\text{abs}}(\mathbf{x}, t)$ is the radiation energy absorbed per unit time and per unit surface area at position $\mathbf{x}$ and time t. Assuming that the radiation field is in thermal equilibrium with the medium through which it propagates [21],

$$\dot{E}_{\text{abs}} = \frac{1}{3}\gamma c Z^3 E^{1/4}. \tag{3b}$$

2.1. Dimensionless formulation

We define a reference energy density E_0 by the relation $\gamma w / E_0^{3/4} = 1.0$, and introduce dimensionless variables and parameters

$$\tilde{\mathbf{x}} = \frac{\mathbf{x}}{w}, \quad \tilde{t} = \frac{tc}{w}, \quad \tilde{\nabla} = w\nabla, \quad \tilde{Z} = \frac{Z}{Z_{\text{hb}}}, \quad \tilde{E} = \frac{E}{Z_{\text{hb}}^4 E_0}. \tag{4}$$

Then (1) takes the dimensionless form

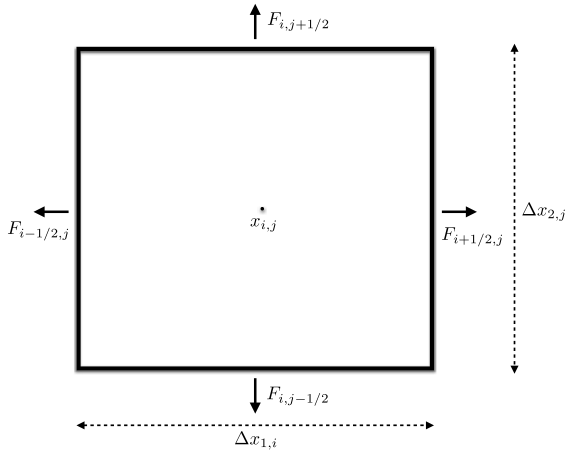

Fig. 2. Cell-centered finite volume discretization of the computational domain $\mathcal{D}$.

$$\frac{\partial \tilde{E}}{\partial \tilde{t}} = \tilde{\nabla} \cdot \left(\frac{\tilde{E}}{\tilde{Z}^3 \tilde{E}^{1/4} + |\tilde{\nabla} \tilde{E}|} \tilde{\nabla} \tilde{E} \right), \qquad \tilde{\mathbf{x}} \in \tilde{\mathcal{D}}. \tag{5}$$

The initial and boundary conditions (2) are transformed in a similar manner. In what follows, we deal only with the dimensionless quantities but omit the tildes $\tilde{\cdot}$ for notational convenience.

2.2. Statistical parametrization

Since the spatial extent and concentration of a contrast agent injected into the brain are always uncertain, we represent $\mathbf{c} = (c_1, c_2)^\top$, the center of the square $\mathcal{D}_2$ occupied by the agent, and Z_2, the concentration-dependent effective atomic number, as random variables.[3] The brain tumor's location $\mathcal{T}$, typically determined via X-ray-based Computed Tomography or Magnetic Resonance Imaging [23], is less uncertain and, hence, is treated deterministically.

To ensure $\mathcal{D}_2 \subset \mathcal{D}$, both c_1 and c_2 must belong to the interval $[w/2, L-w/2]$ or its dimensionless counterpart $[1/2, 9/2]$; in a more realistic scenario, $\mathcal{D}_2$ overlaps with at least one quarter of the tumor region $\mathcal{T}$. We therefore require $c_1 \in [5/2 - c_{\mathrm{H}}, 5/2 + c_{\mathrm{H}}]$ and $c_2 \in [5/2 - c_{\mathrm{V}}, 5/2 + c_{\mathrm{V}}]$ with $0 < c_{\mathrm{H}} \leq 1/2$ and $0 < c_{\mathrm{V}} \leq 1/2$. The minimum and maximum theoretical bounds on the dimensionless effective atomic number Z_2 are 1.0 (no contrast agent) and 10.6 (only contrast agent), respectively. We allow for a more realistic composition of the medium in $\mathcal{D}_2$ by shrinking this interval to $[Z_{\min}, Z_{\max}]$ where $Z_{\min} = 2.0$ and $Z_{\max} = 8.0$. We assume that random variables c_1, c_2 and Z_2 are mutually independent, uniformly distributed on their respective intervals, so that the random vector $\boldsymbol{\xi} = (\xi_1 \equiv c_1, \xi_2 \equiv c_2, \xi_3 \equiv Z_2)^\top$ is characterized by a joint probability density function (PDF)

$$\rho_{\boldsymbol{\xi}}(\mathbf{s}) = \prod_{i=1}^{3} \rho_{\xi_i}(s_i), \qquad \mathbf{s} \in \Lambda, \tag{6}$$

with support $\Lambda = [5/2 - c_{\mathrm{H}}, 5/2 + c_{\mathrm{H}}] \times [5/2 - c_{\mathrm{V}}, 5/2 + c_{\mathrm{V}}] \times [Z_{\min}, Z_{\max}]$, where ρ_{ξ_i} is the marginal uniform PDF of the ith random variable ξ_i $(i = 1, 2, 3)$. The size M of $\boldsymbol{\xi}$ (in our example, $M = 3$) is often referred to as a *stochastic dimension*, and a random solution of (5), $E(\mathbf{x}, t, \boldsymbol{\xi})$, is called a *stochastic response surface*.

3. Numerical algorithm

The response surface $E(\mathbf{x}, t, \boldsymbol{\xi})$ is defined on $\mathcal{D} \times [0, T] \times \Lambda$. Discretization in physical space ($\mathcal{D}$), time ($[0, T]$) and "probability space" (Λ) is discussed below.

3.1. Spatial discretization

The physical domain $\mathcal{D}$ is discretized with a nonuniform mesh, which consists of N grid cells in each spatial direction and is finest within $\mathcal{D}_2 \cup \mathcal{T}$. We employ a cell-centered finite volume (CCFV) approach, in which the fluxes F are defined on the cell boundaries, and E represents the cell-averaged value (Fig. 2). This transforms (5) into a set of ordinary differential equations

[3] Such a parameterization ignores spatiotemporal variability of Z_2, which can arise, e.g., from time-varying injection of the contrast agent during irradiation or spatial variations in the composition of the brain and tumorous tissues.

$$\frac{\mathrm{d}E_{i,j}(t)}{\mathrm{d}t} = -\frac{F_{i+1/2,j}(t) - F_{i-1/2,j}(t)}{\Delta x_i} - \frac{F_{i,j+1/2}(t) - F_{i,j-1/2}(t)}{\Delta x_j}, \tag{7a}$$

where the subscripts $i = 1, \ldots, N$ and $j = 1, \ldots, N$ indicate the position of a cell in the horizontal and vertical directions, respectively, and Δx_i and Δx_j are its dimensions in these respective directions. The flux $F_{i+1/2,j}$ is computed as

$$F_{i+1/2,j} = -2D_{i+1/2,j}\frac{E_{i+1,j} - E_{i,j}}{\Delta x_{i+1} + \Delta x_i}, \tag{7b}$$

where

$$D_{i+1/2,j} = (E_{i+1,j} + E_{i,j})\left(\frac{E_{i+1,j} + E_{i,j}}{D^{\mathrm{h}}_{i+1/2,j}} + 4\frac{|E_{i+1,j} - E_{i,j}|}{\Delta x_{i+1} + \Delta x_i}\right)^{-1} \tag{7c}$$

and $D^{\mathrm{h}}_{i+1/2,j}$ is the harmonic mean of $D_{Z_{i,j}} = Z_{i,j}^{-3}E_{i,j}^{3/4}$ over adjacent cells:

$$D^{\mathrm{h}}_{i+1/2,j} = \frac{\Delta x_i \Delta x_{i+1} D_{Z_{i,j}} D_{Z_{i+1,j}}}{\Delta x_{i+1} D_{Z_{i,j}} + \Delta x_i D_{Z_{i+1,j}}}. \tag{7d}$$

The remaining fluxes $F_{i-1/2,j}$, $F_{i,j+1/2}$ and $F_{i,j-1/2}$ are defined in a similar manner.

Let the subscripts 0 and $N+1$ denote ghost cells, in each of the spatial dimensions, lying along the boundary $\partial\mathcal{D}$, just outside $\mathcal{D}$. These cells are assigned the same dimensions (and the same effective atomic number) as the adjacent cells within $\mathcal{D}$. Then, the boundary conditions (2b)–(2c) are approximated with

$$\frac{E_{0,j} + E_{1,j}}{2} - 2D_{0,j}\frac{E_{1,j} - E_{0,j}}{\Delta x} - 4F_{\mathrm{in}} = 0, \tag{8a}$$

$$\frac{E_{N+1,j} + E_{N,j}}{2} + 2D_{N+1,j}\frac{E_{N+1,j} - E_{N,j}}{\Delta x} - 4F_{\mathrm{out}} = 0, \tag{8b}$$

$$E_{i,0} = E_{i,1}, \qquad E_{i,N+1} = E_{i,N}, \tag{8c}$$

for $i, j = 1, \ldots, N$. Here $D_{0,j}$ and $D_{N+1,j}$ are given by

$$D_{0,j} = \frac{E_{0,j}}{Z_{1,j}^3 E_{0,j}^{1/4} + |E_{1,j} - E_{0,j}|/\Delta x_{1,j}}, \tag{8d}$$

$$D_{N+1,j} = \frac{E_{N+1,j}}{Z_{N,j}^3 E_{N+1,j}^{1/4} + |E_{N+1,j} - E_{N,j}|/\Delta x_{N,j}}. \tag{8e}$$

The Robin boundary conditions are nonlinear equations in $E_{0,j}$ or $E_{N+1,j}$ ($j = 1, \ldots, N$), which are solved iteratively during each time step.

3.2. Time discretization

A first-order implicit Euler method recasts (7) into

$$\frac{E^{n+1}_{i,j} - E^{n}_{i,j}}{\Delta t} = -\frac{F^{n+1}_{i+1/2,j} - F^{n+1}_{i-1/2,j}}{\Delta x_i} - \frac{F^{n+1}_{i,j+1/2} - F^{n+1}_{i,j-1/2}}{\Delta x_j}, \tag{9}$$

where the superscript n indicates discrete time $t_n = n\Delta t$, where Δt is a time step. A Jacobian-free Newton–Krylov (JfNK) solver [24] is used as an iterative procedure for handling the nonlinear terms in the right-hand-side of (9). This avoids the explicit formation of the Jacobian while still benefiting from fast, Newton-like convergence. The time advancement of the solution from t_n to t_{n+1} consists of the following steps:

1. Initialize the Newton iterate by setting $E^{n+1}_{i,j,k=0} = E^{n}_{i,j}$ for all $i, j = 1, \ldots, N$, where k is the iteration number.
2. Inexactly solve the linear system $\mathbf{J}(\mathbf{E}^{n+1}_k)\delta\mathbf{E}_k = -\mathbf{f}(\mathbf{E}^{n+1}_k)$ for the Newton correction $\delta\mathbf{E}_k$ using the Krylov solver GMRES with tolerance ϵ_{K}. The components of $\mathbf{f}$ are given by
$$f_{j\cdot N+i} = \frac{E^{n+1}_{i,j,k} - E^{n}_{i,j}}{\Delta t} + \frac{F^{n+1}_{i+1/2,j,k} - F^{n+1}_{i-1/2,j,k}}{\Delta x_i} + \frac{F^{n+1}_{i,j+1/2,k} - F^{n+1}_{i,j-1/2,k}}{\Delta x_j} \tag{10}$$
for $i, j = 1, \ldots, N$.
3. Perform the Newton step $\mathbf{E}^{n+1}_{k+1} = \mathbf{E}^{n+1}_k + \delta\mathbf{E}_k$ where $\delta\mathbf{E}_k$ is the converged value of the kth Newton correction.
4. Perform steps 2 and 3 until a given tolerance ϵ_{N} is achieved.
5. Advance the solution to t_{n+1} by setting $\mathbf{E}^{n+1} = \mathbf{E}^{n+1}_K$ where K is the number of Newton iterations at convergence.

Details on our implementation of step 2 are provided in Appendix B.

Finally, the dimensionless total energy deposition in the tumorous region $\mathcal{T}$ during $(0, T]$ is given by (see Appendix A)

$$E_{\text{tot}} = \frac{\Delta t}{3} \sum_{i=1}^{I} \sum_{j} \sum_{k} Z_{j,k}^3 (E_{j,k}^{i+1})^{1/4} \Delta x_{1,j} \Delta x_{2,k}, \tag{11}$$

where the sum is over the indices j and k corresponding to the grid cells located within $\mathcal{T}$. Since the nonuniform grid resulting from the CCFV discretization does not necessarily align with the boundary $\partial\mathcal{T}$ of $\mathcal{T}$, we define a uniform interpolation grid with $\Delta x_1^u = \Delta x_2^u = 5/N$ that exactly lines up with $\partial\mathcal{T}$, and use the interpolated values of E and Z on this new grid to calculate E_{tot}. A cubic spline interpolation for E and linear interpolation for Z was found to be optimal. The total energy deposition in $\mathcal{T}$ is then computed as

$$E_{\text{tot}} = \frac{\Delta t \Delta x_1^u \Delta x_2^u}{3} \sum_{i=1}^{I} \sum_{j=N_1^u+1}^{N_1^u+N_2^u} \sum_{k=N_1^u+1}^{N_1^u+N_2^u} Z_{j,k}^3 (E_{j,k}^{i+1})^{1/4}, \tag{12}$$

where $N_1^u = 2N/5$ and $N_2^u = N/5$.

3.3. Monte Carlo simulation and stochastic collocation

Statistical moments of $E(\mathbf{x}, t, \boldsymbol{\xi})$, or a QoI derived from E, are its weighted (with $\rho_{\boldsymbol{\xi}}$) integrals over the support Λ of $\boldsymbol{\xi}$. For example, the ensemble mean and variance of E_{tot}, the energy deposited in the tumor over time T, are defined, respectively, by

$$\langle E_{\text{tot}} \rangle = \int_{\Lambda} E_{\text{tot}}(\mathbf{s}) \rho(\mathbf{s}) \mathrm{d}\mathbf{s} \quad \text{and} \quad \sigma_{E_{\text{tot}}}^2 = \int_{\Lambda} E_{\text{tot}}^2(\mathbf{s}) \rho(\mathbf{s}) \mathrm{d}\mathbf{s} - \langle E_{\text{tot}} \rangle^2. \tag{13}$$

Monte Carlo estimates of these quantities are

$$\hat{E}_{\text{tot}}^{\text{MC}} = \frac{1}{N_{\text{sam}}} \sum_{i=1}^{N_{\text{sam}}} E_{\text{tot}}(\boldsymbol{\eta}_i) \quad \text{and} \quad \hat{\sigma}_{E_{\text{tot}}}^{2,\text{MC}} = \frac{1}{N_{\text{sam}}} \sum_{i=1}^{N_{\text{sam}}} [E_{\text{tot}}(\boldsymbol{\eta}_i)]^2 - [\hat{E}_{\text{tot}}^{\text{MC}}]^2. \tag{14}$$

Here $\{\boldsymbol{\eta}_i\}_{i=1}^{N_{\text{sam}}}$ is a set of N_{sam} realizations of $\boldsymbol{\xi}$ sampled from (6). The MCS estimation error for the mean, $\mathcal{E}_{\text{est}}^{\text{MC}} \equiv |\langle E_{\text{tot}} \rangle - \hat{E}_{\text{tot}}^{\text{MC}}|$, is independent of the stochastic dimension M but has a slow decay rate of $\sigma_{E_{\text{tot}}}/\sqrt{N_{\text{sam}}}$.

Stochastic collocation (SC) aims to achieve faster convergence through the use of better quadrature rules to approximate the weighted integrals in (13),

$$\hat{E}_{\text{tot}}^{\text{SC}} = \sum_{i=1}^{P} w_i \, E_{\text{tot}}(\mathbf{s}_i) \quad \text{and} \quad \hat{\sigma}_{E_{\text{tot}}}^{2,\text{SC}} = \sum_{i=1}^{P} w_i \, [E_{\text{tot}}(\mathbf{s}_i)]^2 - [\hat{E}_{\text{tot}}^{\text{SC}}]^2. \tag{15}$$

Here $\mathbf{s}_i$ and w_i are the nodes and weights of the quadrature formula, respectively; and P is the number of nodes. The goal of SC is to achieve the same estimation error as MCS by using $P < N_{\text{sam}}$ collocation nodes. Since our uncertain parameters have uniform distributions, we employ the Clenshaw–Curtis quadrature rule [25,26], whose nodes and weights are rescaled from the standard interval $[-1, 1]$ to the actual parameter ranges.

For stochastic dimension $M > 1$, *product* or *tensor grid* rules may be constructed through the tensor product of M univariate rules [27]. The number of nodes in such grids increases exponentially with M, i.e., for $k+1$ nodes in each dimension it behaves like $(k+1)^M$ (the so-called "curse of dimensionality"). Instead, *sparse grid* rules may be built from univariate rules using the Smolyak algorithm [28], whose number of nodes increases approximately as $(2M)^k/k!$, i.e., polynomially with M. We adopt the latter approach with univariate Clenshaw–Curtis quadrature rules [29], as implemented by Burkardt in MATLAB.

4. Simulation results and discussion

We discretize the simulation domain $(0, 5) \times (0, 5)$ into $N = 20$ grid cells in each direction, and the time horizon $(0, T = 1.0)$ with $\Delta t = 0.5 \times 10^{-2}$ time steps.[4] We set $E_{\text{in}} = 5.0$, $F_{\text{in}} = 20.0$ and $F_{\text{out}} = 0$; the latter condition corresponds to a vacuum boundary, and ignores any black-body radiation emitted by the medium surrounding the brain near the exit point of the radiation. The JfNK coupling has a convergence tolerance of $\epsilon_{\text{N}} = 10^{-3}$ for the Newton iteration and $\epsilon_{\text{K}} = 10^{-3}$ for the GMRES algorithm. The computations were performed on an Intel Core i7 machine running at 4 GHz.

[4] Numerical experiments using longer time horizons yielded similar results for the comparison between SC and MCS, and for the influence of the statistical moments of the uncertain parameters on those of the total energy deposition in the tumor.

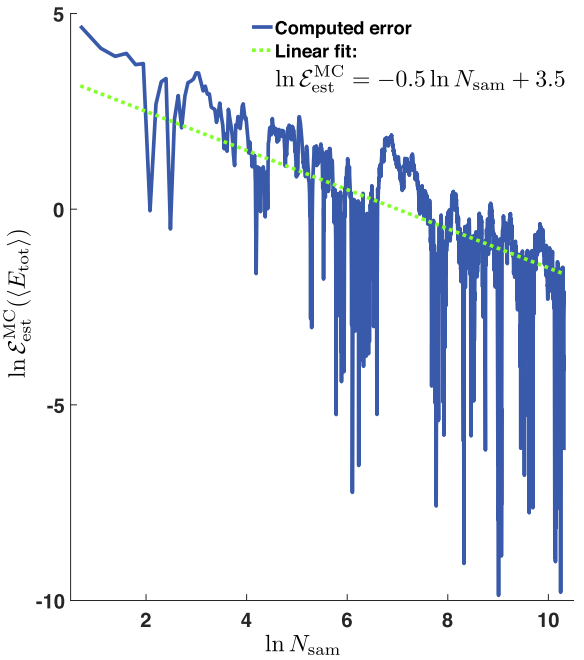

Fig. 3. Monte Carlo estimation error $\mathcal{E}_{\text{est}}^{\text{MC}}(\langle E_{\text{tot}} \rangle)$ as a function of the number of MC realizations N_{sam}. Ranges of variability of the $M = 3$ random parameters $\boldsymbol{\xi}$ are defined by $c_{\text{H}} = c_{\text{V}} = 0.5$ and $[Z_{\min}, Z_{\max}] = [2, 8]$.

We define the estimation errors

$$\mathcal{E}_{\text{est}}^{p}(\langle E_{\text{tot}} \rangle) = |\hat{E}_{\text{tot}}^{p} - \hat{E}_{\text{tot}}^{\text{ref}}| \quad \text{and} \quad \mathcal{E}_{\text{est}}^{p}(\sigma_{E_{\text{tot}}}^{2}) = |\hat{\sigma}_{E_{\text{tot}}}^{2,p} - \hat{\sigma}_{E_{\text{tot}}}^{2,\text{ref}}|, \tag{16}$$

for the moments' estimates computed with SC ($p = \text{SC}$) and MCS ($p = \text{MC}$). The reference values of these moments, $\hat{E}_{\text{tot}}^{\text{ref}}$ and $\hat{\sigma}_{E_{\text{tot}}}^{2,\text{ref}}$, are computed with $N_{\text{sam}}^{\text{ref}} = 30000$ Monte Carlo realizations in all of our numerical experiments except for those with two uncertain parameters c_1 and Z_2, where 35000 samples were used. Fig. 3 demonstrates that $\mathcal{E}_{\text{est}}^{\text{MCS}}(\langle E_{\text{tot}} \rangle) \sim N_{\text{sam}}^{-0.5}$, as expected from theory [30].

We investigate the relative performance of SC and MCS in terms of its convergence rate for the mean, i.e., whether the numbers of deterministic solves, P and N_{sam}, necessary to achieve the relative estimation error $\mathcal{E}_{\text{est}}^{p}(\langle E_{\text{tot}} \rangle)/\hat{E}_{\text{tot}}^{\text{ref}} \sim \mathcal{O}(10^{-3})$ for $p = \text{SC}$ and MC satisfy $P < N_{\text{sam}}$. Since the performance of SC is known to deteriorate with the stochastic dimension M, we conduct a series of numerical experiments for $M = 1$ (either c_1 or Z_2 is random), $M = 2$ (both c_1 and Z_2 are random), and $M = 3$ (c_1, c_2 and Z_2 are random).

4.1. One stochastic dimension ($M = 1$)

We start by considering the impact of a single random parameter, either $c_1 \in [2.0, 3.0]$ with $c_2 = 2.5$ and $Z_2 = 6.0$ or $Z_2 \in [2.0, 8.0]$ with $c_1 = c_2 = 2.5$, on the relative performance of SC and MCS. Fig. 4 demonstrates that SC outperforms MCS by at least one order of magnitude when c_1 is random (Fig. 4a) and by several orders of magnitude when Z_2 is random (Fig. 4b). The convergence criterion $\mathcal{E}_{\text{est}}^{\text{SC}}(\langle E_{\text{tot}} \rangle)/\hat{E}_{\text{tot}}^{\text{ref}} \sim \mathcal{O}(10^{-3})$ is achieved with $P = 65$ and 9 in the former and latter cases, respectively.

Fig. 5 exhibits the impact of uncertainty in either c_1 or Z_2 (as quantified by their respective coefficients of variation CV_{c_1} and CV_{Z_2}) on both predictions of energy deposition, $\hat{E}_{\text{tot}}^{\text{SC}}$, and predictive uncertainty expressed in terms of $\text{CV}_{E_{\text{tot}}} = \hat{\sigma}_{E_{\text{tot}}}^{\text{SC}}/\hat{E}_{\text{tot}}^{\text{SC}}$. The energy deposition $\hat{E}_{\text{tot}}^{\text{SC}}$ decreases with CV_{c_1} (or, for a fixed $\langle c_1 \rangle$, with σ_{c_1}); this is to be expected since increasing σ_{c_1} causes the region $\mathcal{D}_2$ to overlap less with the tumor region $\mathcal{T}$, thereby diminishing the dose-enhancing effect of the contrast agent. A relatively small input uncertainty, $\text{CV}_{c_1} = 0.12$, reduces the energy absorption by 27% relative to the ideal (deterministic) situation of full overlap between $\mathcal{D}_2$ and $\mathcal{T}$ and $Z_2 = 6.0$ (Fig. 5a). On the contrary, increasing CV_{Z_2} (or, for a fixed $\langle Z_2 \rangle = 5.0$, increasing σ_{Z_2}) causes the energy deposition $\hat{E}_{\text{tot}}^{\text{SC}}$ to increase (Fig. 5b), as higher values of Z_2 are sampled and the probability of photo-electric absorption of the X-rays increases with atomic number. The parametric uncertainty characterized by $\sigma_{Z_2} = 0.35$ enhances the energy absorption by 36% relative to the aforementioned ideal (deterministic) situation.

Fig. 5 also demonstrates the impact of parametric uncertainty, CV_{c_1} in Fig. 5a and CV_{Z_2} in Fig. 5b, on predictive uncertainty, $\text{CV}_{E_{\text{tot}}}$. In both cases, even small uncertainty in a single parameter gives rise to appreciable predictive uncertainty and, hence, should not be ignored.

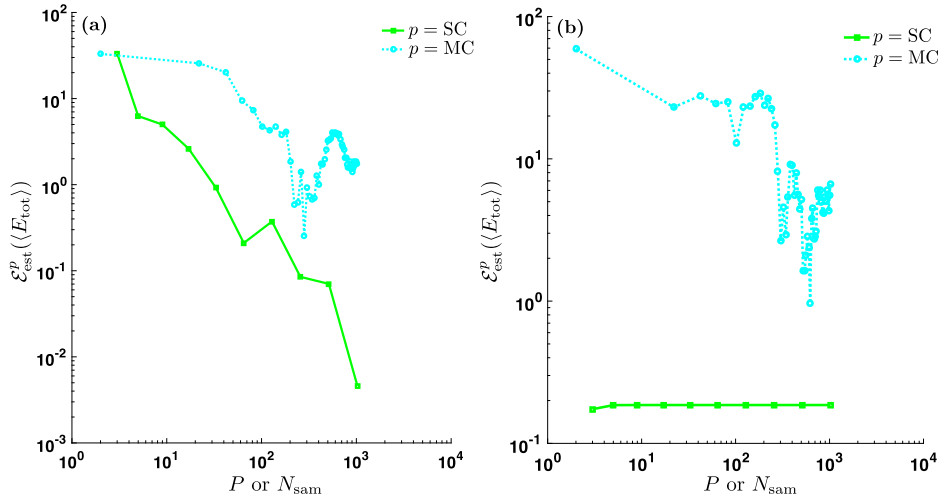

Fig. 4. Error in estimation of the mean energy deposition in the tumor, $\mathcal{E}^p_{\mathrm{est}}(\langle E_{\mathrm{tot}}\rangle)$, as a function of the number of collocation nodes (P) in SC or MC samples (N_{sam}) in MCS, when only one parameter is uncertain ($M = 1$): either c_1 (left) or Z_2 (right).

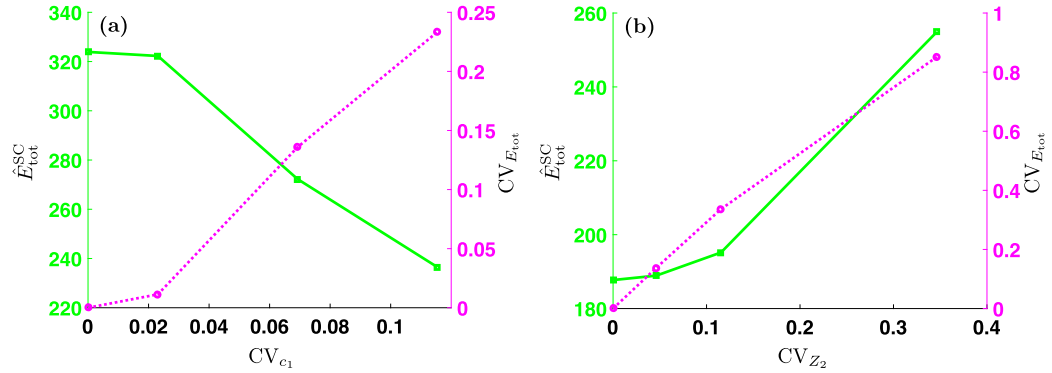

Fig. 5. Dependence of the mean ($\hat{E}^{\mathrm{SC}}_{\mathrm{tot}}$) and coefficient of variation ($\mathrm{CV}_{E_{\mathrm{tot}}}$) of the total energy deposition on the coefficient of variation of a single ($M = 1$) uncertain parameter, either (a) CV_{c_1} of c_1 or (b) CV_{Z_2} of Z_2.

4.2. Multiple stochastic dimensions ($M = 2$ and 3)

To investigate the relative performance of SC and MCS further, we increase the number of random input parameters from $M = 1$ (Section 4.1) to $M = 2$ and 3. The former case involves two random parameters $c_1 \in [2.0, 3.0]$ and $Z_2 \in [2.0, 8.0]$ with fixed $c_2 = 5/2$, and the latter three random parameters $c_1 \in [2.0, 3.0]$, $Z_2 \in [2.0, 8.0]$ and $c_2 \in [2.0, 3.0]$. Fig. 6 reveals that SC outperforms MCS only marginally, with the difference between the two diminishing as M increases from two (Fig. 6a) to three (Fig. 6b), as the number of collocation points necessary to achieve the convergence criterion $\mathcal{E}^{\mathrm{SC}}_{\mathrm{est}}(\langle E_{\mathrm{tot}}\rangle)/\hat{E}^{\mathrm{ref}}_{\mathrm{tot}} \sim \mathcal{O}(10^{-3})$ grows from $P = 321$ to $P = 1073$. This performance is a reflection of the highly irregular stochastic response surface; it is likely to deteriorate further as the degree of parametric uncertainty, quantified by coefficients of variation of the input parameters, increases [17].

Fig. 7 illustrates the combined effect of the two uncertain parameters c_1 and Z_2 (the $M = 2$ case described above) on the mean and CV of the total energy deposition. The results are mostly a combination of those reported in Section 4.1, with a maximum decrease in energy absorption of 35% relative to the aforementioned ideal (deterministic) situation (Fig. 7a). This is higher than the maximum relative deviation due to uncertainty in c_1 only, but slightly lower than that due to uncertainty solely in Z_2. That is because of the counteracting effects of increasing $\sigma^2_{c_1}$ and increasing $\sigma^2_{Z_2}$ on the mean energy absorption. Although not shown here the maximum discrepancy between the model with the three uncertain parameters ($M = 3$) and the ideal (deterministic) case is 46%. Both two (Fig. 7b) and three (not shown) random parameters give rise to a maximum value of $\mathrm{CV}_{E_{\mathrm{tot}}}$ that is close to 1, i.e., uncertainty in the prediction of energy deposition approximately equals the prediction (mean value) itself.

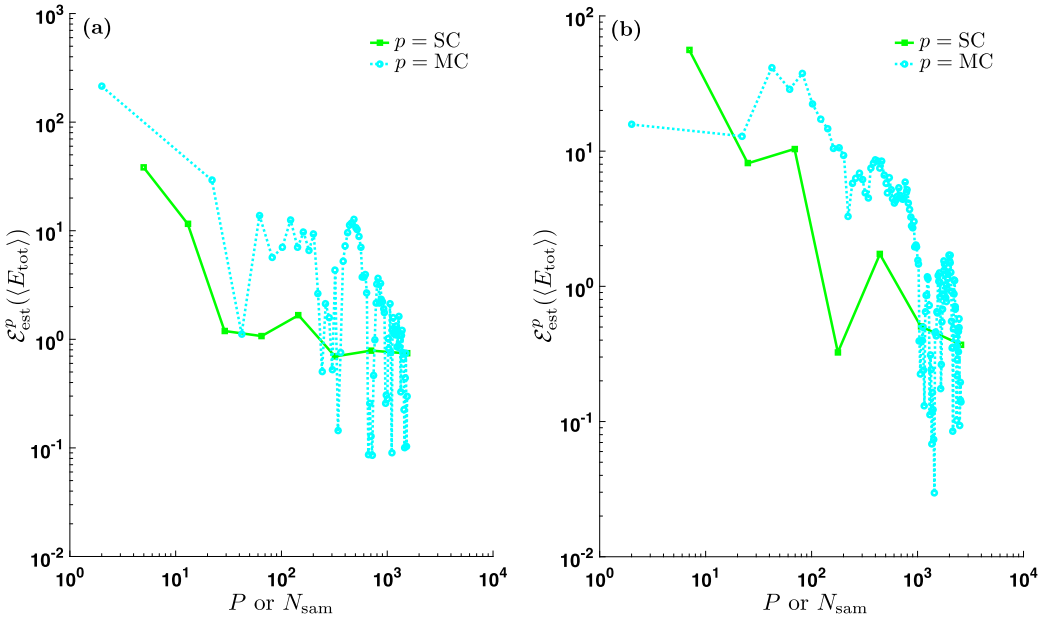

Fig. 6. Error in estimation of the mean energy deposition in the tumor, $\mathcal{E}^p_{\mathrm{est}}(\langle E_{\mathrm{tot}}\rangle)$, as a function of the number of collocation nodes (P) in SC or MC samples (N_{sam}) in MCS, for (a) two and (b) three uncertain parameters, i.e., $M = 2$ and 3, respectively.

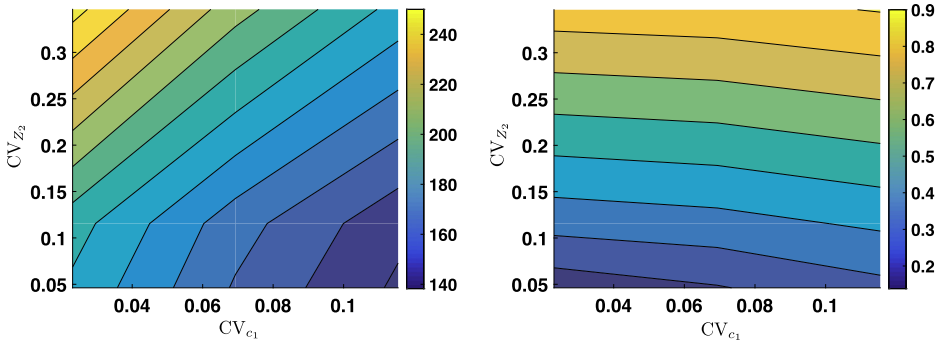

Fig. 7. Dependence of the mean ($\hat{E}^{\mathrm{SC}}_{\mathrm{tot}}$) (a) and coefficient of variation ($\mathrm{CV}_{E_{\mathrm{tot}}}$) (b) of the total energy deposition on the coefficients of variation of two uncertain parameters ($M = 2$), CV_{c_1} and CV_{Z_2}.

5. Global sensitivity analysis

The rapid degradation in the relative performance of SC puts a premium on reduction of the problem's stochastic dimension. We accomplish this goal by employing the global sensitivity analysis of Sobol' [31], which decomposes a model output variance into summands of variances of input parameters and, hence, quantifies the contribution of each input parameter and its interactions with other parameters to the overall model output variance. In particular, first-order sensitivity indices are defined as [31–33]

$$S_{c_1} = \frac{\sigma^2_{E_{\mathrm{tot}},c_1}}{\sigma^2_{E_{\mathrm{tot}}}}, \quad S_{c_2} = \frac{\sigma^2_{E_{\mathrm{tot}},c_2}}{\sigma^2_{E_{\mathrm{tot}}}}, \quad S_{Z_2} = \frac{\sigma^2_{E_{\mathrm{tot}},Z_2}}{\sigma^2_{E_{\mathrm{tot}}}}, \tag{17}$$

where $\sigma^2_{E_{\mathrm{tot}},c_1}$ represents the contribution of c_1 to the total variance of E_{tot}, and likewise for c_2 and Z_2. Total-order sensitivity indices are given by

$$S^{\mathrm{tot}}_{c_1} = \frac{1}{\sigma^2_{E_{\mathrm{tot}}}} \sum_{\alpha\in\mathcal{I}_{c_1}} \sigma^2_\alpha, \quad S^{\mathrm{tot}}_{c_2} = \frac{1}{\sigma^2_{E_{\mathrm{tot}}}} \sum_{\alpha\in\mathcal{I}_{c_2}} \sigma^2_\alpha, \quad S^{\mathrm{tot}}_{Z_2} = \frac{1}{\sigma^2_{E_{\mathrm{tot}}}} \sum_{\alpha\in\mathcal{I}_{Z_2}} \sigma^2_\alpha, \tag{18}$$

where $\mathcal{I}_{c_1}$ is the set of all subsets of $\{c_1, c_2, Z_2\}$ containing c_1, and likewise for $\mathcal{I}_{c_2}$ and $\mathcal{I}_{Z_2}$. To compute (17) and (18), either MCS [32], polynomial chaos [33] or stochastic collocation [34] may be used; we employ MCS implemented via a combination of our numerical solver and the MATLAB code in [35].

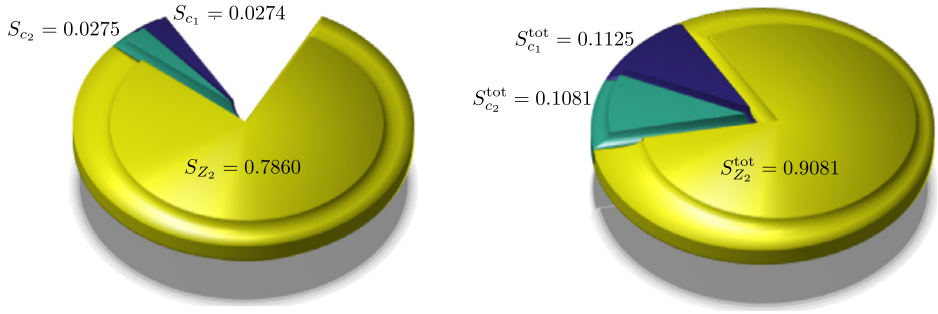

Fig. 8. First-order (left) and total-order (right) Sobol' indices for three random parameters ($M = 3$): $c_1 \in [2.0, 3.0]$, $c_2 \in [2.0, 3.0]$ and $Z_2 \in [2.0, 8.0]$.

Fig. 8 shows that $S_{c_1} \approx S_{c_2}$, in line with the fact that a similar change in c_1 and c_2 causes a similar deviation of the contrast-agent region $\mathcal{D}_2$ from the tumor region $\mathcal{T}$; the first-order index for Z_2 is much larger, indicating that variations in the atomic number have a much larger effect on the predictive uncertainty of the total energy deposition in $\mathcal{T}$ than changes in c_1 or c_2. This may be understood from the nonlinear (cubic) dependence of the energy deposition on the effective atomic number, as illustrated by (11). Fig. 8 also reveals a clear difference between the total-order Sobol' indices for c_1, c_2 and Z_2 and their first-order counterparts, indicating that there is a measurable impact of the interactions between the different parameters on the total variance in E_{tot}.

6. Summary and conclusions

We estimated the energy deposition into a brain tumor irradiated by X-rays in the presence of parametric uncertainty using the stochastic collocation (SC) approach. We represented the uncertain input parameters, namely the coordinates of the center of the region containing an iodinated, dose-enhancing contrast agent, and the effective value of the atomic number in this area, as mutually independent, uniformly distributed random variables. We investigated the effect of changes in their mean and/or variance on the statistical moments of the deposited energy, and compared the computational efficiency of SC to that of standard Monte Carlo simulation (MCS).

Our analysis leads to the following major conclusions:

1. SC is at least an order of magnitude faster than MCS when only one parameter is uncertain/random. In the presence of multiple uncertain parameters, SC outperforms MCS only marginally, with the difference between the two diminishing as the number of parameters increases from two to three.
2. In the majority of cases, the problem's nonlinearity amplifies the coefficient of variation of the uncertain parameters, yielding a larger coefficient of variation for the energy deposition. Hence, even small parametric uncertainties may result in large predictive uncertainty in the quantity of interest.
3. As the stochastic dimension increases, the magnitude of the predictive uncertainty in the energy deposition, as measured by its standard deviation, approaches that of the prediction (mean energy deposition) itself.
4. In the presence of additional uncertain parameters, the effect of uncertainty in a specific parameter on the predictive uncertainty in the quantity of interest may differ from its effect when this parameter is the only uncertain input.
5. A global sensitivity analysis reveals that predictive uncertainty in the energy deposition is mainly influenced by variations in the effective atomic number, and is also affected by interactions between the different uncertain parameters.

The flux-limited radiation–diffusion approximation employed to model the propagation of X-rays within the brain has also been applied to a wide range of other problems including core collapse supernovae [36] and inertial confinement fusion [37]. Hence, our findings are relevant to the quantification of predictive uncertainty across a number of research areas. Future extensions of the presented analysis include considering a three-dimensional model with a larger number of uncertain parameters which exhibit spatiotemporal variability, and representing the latter by random variables with more complex probability distributions.

Acknowledgements

We would like to thank Jim Morel, Michael Holst and Maxime Theillard for helpful discussions. This work was supported in part by Defense Advanced Research Projects Agency under the EQUiPS program.

Appendix A. Derivation of the total energy deposition in the tumor

For a particular realization of the random parameter vector $\boldsymbol{\xi}$, the dimensionless energy absorption per unit time and unit surface area at position $\mathbf{x}$ and time t is given by [21],

$$\dot{\tilde{E}}_{\text{abs}} = \frac{w}{E_0 c Z_1^4}\dot{E}_{\text{abs}} = \frac{\gamma w}{3E_0^{3/4}}\tilde{Z}^3\tilde{E}^{1/4} = \frac{1}{3}\tilde{Z}^3\tilde{E}^{1/4}, \tag{A.1}$$

where E_0, $\tilde{Z}$ and $\tilde{E}$ are defined in Section 2. To obtain the energy absorption $E_{\text{abs}}(i,j,k)$ in $\mathbf{\Delta}x_{j,k} \equiv [x_{1,j} - \Delta x_{1,j}/2, x_{1,j} + \Delta x_{1,j}/2] \times [x_{2,k} - \Delta x_{2,k}/2, x_{2,k} + \Delta x_{2,k}/2]$ during the time step Δt from t_i to $t_i + \Delta t$ ($i = 0, \ldots, I-1$ with $I = T/\Delta t$ and $t_0 = 0$), where $\Delta x_{1,j}$ and $\Delta x_{2,k}$ ($j,k = 1,\ldots,N$) are the dimensions in spatial directions 1 and 2, respectively, of the grid cell centered around $(x_{1,j}, x_{2,k})^\top$, we multiply $\dot{E}_{\text{abs}}(i,j,k)$ with $\Delta t \Delta x_{1,j}\Delta x_{2,k}$. In analogy with (A.1), we define a corresponding dimensionless quantity

$$\tilde{E}_{\text{abs}}(i,j,k) = \frac{1}{3}\tilde{Z}_{j,k}^3(\tilde{E}_{j,k}^{i+1})^{1/4}\Delta\tilde{t}\Delta\tilde{x}_{1,j}\Delta\tilde{x}_{2,k}, \tag{A.2}$$

with $\Delta\tilde{t} = c\Delta t/w$, $\Delta\tilde{x}_{1,j} = \Delta x_{1,j}/w$ and $\Delta\tilde{x}_{2,k} = \Delta x_{2,k}/w$. Here $\tilde{Z}_{j,k}$ is the value of $\tilde{Z}$ in $\mathbf{\Delta}\tilde{x}_{j,k}$ (we assume that $\tilde{Z}$ is constant over a finite volume cell) and $\tilde{E}_{j,k}^{i+1}$ approximates the average value of the dimensionless radiation energy density over $\mathbf{\Delta}\tilde{x}_{j,k}$ during the dimensionless time step from $\tilde{t}_i$ to $\tilde{t}_i + \Delta\tilde{t}$ (we evaluate it at $\tilde{t}_i + \Delta\tilde{t}$). The dimensionless total energy absorption $\tilde{E}_{\text{abs,tot}}$ by the medium in the entire region $\tilde{\mathcal{T}}$ over time $\tilde{T} = I\Delta\tilde{t}$ is then given by

$$\tilde{E}_{\text{tot}} = \sum_{i=1}^{I}\sum_{j}\sum_{k}\tilde{E}_{\text{abs}}(i,j,k), \tag{A.3}$$

where we sum over the indices j and k corresponding to the grid cells within $\tilde{\mathcal{T}}$. Together with (A.2), and omitting $\tilde{\cdot}$, this yields

$$E_{\text{tot}} = \frac{\Delta t}{3}\sum_{i=1}^{I}\sum_{j}\sum_{k}Z_{j,k}^3(E_{j,k}^{i+1})^{1/4}\Delta x_{1,j}\Delta x_{2,k}. \tag{A.4}$$

Appendix B. Implementation of Krylov algorithm for Newton corrections

Despite its quadratic convergence rate, a standard Newton method requires computation of the full Jacobian **J**. For our radiation–diffusion problem, the derivatives in **J** cannot be obtained analytically and instead would need to be approximated numerically (e.g., using Fréchet derivatives). Rather than pursuing this approach, which is prone to errors and also time-consuming, we solve the linear system $\mathbf{J}(\mathbf{E}_k^{n+1})\delta\mathbf{E}_{k+1} = -\mathbf{f}(\mathbf{E}_k^{n+1})$, where $J_{i,j} = \partial f_i/\partial E_j$, at the kth Newton iteration inexactly using the iterative Krylov algorithm *Generalized Minimum RESidual (GMRES)*.[5] To implement this method we only need to represent the Jacobian-vector product **Jv**, where **v** is the Krylov vector, rather than explicitly calculate the Jacobian matrix elements. Specifically, **Jv** is approximated by finite differences with either first-order accuracy [24]

$$\mathbf{J}(\mathbf{E}_k^{n+1})\mathbf{v} \approx \frac{\mathbf{f}(\mathbf{E}_k^{n+1} + \varepsilon\mathbf{v}) - \mathbf{f}(\mathbf{E}_k^{n+1})}{\varepsilon}, \tag{B.1}$$

or second-order accuracy [24]

$$\mathbf{J}(\mathbf{E}_k^{n+1})\mathbf{v} \approx \frac{\mathbf{f}(\mathbf{E}_k^{n+1} + \varepsilon\mathbf{v}) - \mathbf{f}(\mathbf{E}_k^{n+1} - \varepsilon\mathbf{v})}{2\varepsilon}. \tag{B.2}$$

Here ε is a small perturbation parameter, which cannot be too large (poor derivative approximation) or too small (large floating-point roundoff error). Omitting the subscript k and superscript $n+1$ for notational convenience, we use

$$\varepsilon = \begin{cases} \dfrac{1}{n\|\mathbf{v}\|_2}\displaystyle\sum_{i=1}^{n}\sqrt{\epsilon}(1+|E_i|) & \text{if } \|\mathbf{v}\|_2 > \epsilon \\ \dfrac{1}{n}\displaystyle\sum_{i=1}^{n}\sqrt{\epsilon}(1+|E_i|) & \text{if } \|\mathbf{v}\|_2 \le \epsilon, \end{cases} \tag{B.3}$$

where n is the size of **E** ($n = N^2$ for N grid cells in each spatial direction) and $\epsilon = 2.2204 \times 10^{-16}$ (machine epsilon for 64-bit double precision). Our simulations employ (B.2).

[5] Here we reshaped the two-dimensional matrix $\mathbf{E}_k^{n+1}$ into a one-dimensional array, and then reshaped the converged solution $\mathbf{E}_K^{n+1}$ back into a two-dimensional matrix.

References

[1] A. Norman, K.S. Iwamoto, S.T. Cochran, Iodinated contrast agents for brain tumor localization and radiation dose enhancement, Invest. Radiol. 26 (Suppl. 1) (1991) S120–S121, discussion, S125–128.
[2] A. Macovski, Medical Imaging Systems, Prentice-Hall, New Jersey, 1983.
[3] H. Elleaume, A.-M. Charvet, S. Corde, F. Estève, J.-F. Le Bas, Performance of computed tomography for contrast agent concentration measurements with monochromatic X-ray beams: comparison of K-edge versus temporal subtraction, Phys. Med. Biol. 47 (2002) 3369–3385.
[4] C.S. Hamilton, M.A. Ebert, Volumetric uncertainty in radiotherapy, Clin. Oncol. 17 (6) (2005) 456–464.
[5] C. Beltran, M. Naik, T.E. Merchant, Dosimetric effect of target expansion and setup uncertainty during radiation therapy in pediatric craniopharyngioma, Radiother. Oncol. 97 (3) (2010) 399–403.
[6] H. Paganetti, Range uncertainties in proton therapy and the role of Monte Carlo simulations, Phys. Med. Biol. 57 (11) (2012) R99–R117.
[7] E. Seravalli, P.M. van Haaren, P.P. van der Toorn, C.W. Hurkmans, A comprehensive evaluation of treatment accuracy, including end-to-end tests and clinical data, applied to intracranial stereotactic radiotherapy, Radiother. Oncol. 116 (1) (2015) 131–138.
[8] L. Million, M. Axente, Pediatric cancers, in: Y. Nishimura, R. Komaki (Eds.), Intensity-Modulated Radiation Therapy, Springer, Japan, 2015, pp. 443–465, Ch. 22.
[9] T.D. Solberg, K.S. Iwamoto, A. Norman, Calculation of radiation dose enhancement factors for dose enhancement therapy of brain tumors, Phys. Med. Biol. 37 (1992) 439–443.
[10] A.V. Mesa, A. Norman, T.D. Solberg, J.J. Demarco, J.B. Smathers, Dose distributions using kilovoltage X-rays and dose enhancement from iodine contrast agents, Phys. Med. Biol. 44 (1999) 1955–1968.
[11] E.D. Cashwell, C.J. Everett, A Practical Manual on the Monte Carlo Method for Random Walk Problems, Pergamon Press, London, 1959.
[12] X-5 Monte Carlo Team, MCNP – A General Monte Carlo N-Particle Transport Code, Version 5, Volume I: Overview and Theory, LA-UR-03-1987, Los Alamos National Laboratory, 2008.
[13] D.M. Tartakovsky, A. Guadagnini, M. Riva, Stochastic averaging of nonlinear flows in heterogeneous porous media, J. Fluid Mech. 492 (2003) 47–62.
[14] R.G. Ghanem, P.D. Spanos, Stochastic Finite Elements: A Spectral Approach, Springer-Verlag, New York, 1991.
[15] D. Xiu, J.S. Hesthaven, High order collocation methods for differential equations with random inputs, SIAM J. Sci. Comput. 27 (3) (2005) 1118–1139.
[16] M.B. Giles, Multilevel Monte Carlo path simulation, Oper. Res. 56 (3) (2008) 607–617.
[17] D.A. Barajas-Solano, D.M. Tartakovsky, Stochastic collocation methods for nonlinear parabolic equations with random coefficients, SIAM/ASA J. Uncertain. Quantificat. 4 (1) (2016) 475–494.
[18] C.D. Levermore, G.C. Pomraning, A flux-limited diffusion theory, Astrophys. J. 248 (1981) 321–334.
[19] D. Mihalas, B. Weibel-Mihalas, Foundations of Radiation Hydrodynamics, 1st edition, Oxford Univ. Press, New York, 1984.
[20] J.-F. Adam, H. Elleaume, A. Joubert, M.-C. Biston, A.-M. Charvet, J. Balosso, J.-F. Le Bas, F. Estève, Synchrotron radiation therapy of malignant brain glioma loaded with an iodinated contrast agent: first trial on rats bearing F98 gliomas, Int. J. Radiat. Oncol. Biol. Phys. 57 (5) (2003) 1413–1426.
[21] W.J. Rider, D.A. Knoll, G.L. Olson, A multigrid Newton–Krylov method for multimaterial equilibrium radiation diffusion, J. Comput. Phys. 152 (1999) 164–199.
[22] S. Ramu, Effective atomic numbers for photon energy absorption and photon attenuation of tissues from human organs, Med. Dosim. 27 (1) (2002) 1–9.
[23] D. Bhattacharyya, T. Kim, Brain tumor detection using MRI image analysis, in: Ubiquitous Computing and Multimedia Applications: Second International Conference, UCMA 2011, Daejeon, Korea, April 13–15, 2011.
[24] D.A. Knoll, D.E. Keyes, Jacobian–free Newton–Krylov methods: a survey of approaches and applications, J. Comput. Phys. 193 (2004) 357–397.
[25] D. Xiu, Numerical Methods for Stochastic Computations: A Spectral Method Approach, Princeton University Press, Princeton, NJ, 2010.
[26] H. Engels, Numerical Quadrature and Cubature, Academic Press, London, 1980.
[27] E. Novak, K. Ritter, Simple cubature formulas with high polynomial exactness, Constr. Approx. 15 (1999) 499–522.
[28] S.A. Smolyak, Quadrature and interpolation formulas for tensor products of certain classes of functions, Dokl. Akad. Nauk SSSR 4 (1963) 240–243.
[29] F. Nobile, R. Tempone, C. Webster, A sparse grid stochastic collocation method for partial differential equations with random input data, SIAM J. Numer. Anal. 46 (5) (2008) 2309–2345.
[30] M.H. Kalos, P.A. Whitlock, Monte Carlo Methods, 2nd edition, Wiley–VCH, Weinheim, 2008.
[31] I.M. Sobol', Sensitivity estimates for nonlinear mathematical models, Math. Model. Comput. Exp. 1 (1993) 407–414.
[32] I.M. Sobol', Global sensitivity indices for nonlinear mathematical models and their Monte Carlo estimates, Math. Comput. Simul. 55 (2001) 271–280.
[33] B. Sudret, Global sensitivity analysis using polynomial chaos expansions, Reliab. Eng. Syst. Saf. 93 (2008) 964–979.
[34] G.T. Buzzard, D. Xiu, Variance-based global sensitivity analysis via sparse-grid interpolation and cubature, Commun. Comput. Phys. 9 (3) (2010) 542–567.
[35] N. Bilal, Implementation of Sobol's method of global sensitivity analysis to a compressor simulation model, in: 22nd International Compressor Engineering Conference at Purdue, July 14–17, 2014.
[36] A. Mezzacappa, A.C. Calder, S.W. Bruenn, J.M. Blondin, M.W. Guidry, M.R. Strayer, A.S. Umar, An investigation of neutrino-driven convection and the core collapse supernova mechanism using multigroup neutrino transport, Astrophys. J. 495 (1998) 911–926.
[37] J.J. Duderstadt, G.A. Moses, Inertial Confinement Fusion, John Wiley and Sons, New York, 1982.